Three port photonic and plasmonic demultiplexers based on Cross and U-shaped stub structures: Application for filtering and sensing

S. Khattou, M. Amrani, A. Mouadili, E. El Boudouti, Abdelkrim Talbi, Abdellatif Akjouj, Bahram Djafari-Rouhani

Journal of Applied Physics ARTICLE scitation.org/journal/jap

Three port photonic and plasmonic demultiplexers based on Cross and U-shaped stub structures: Application for filtering and sensing

Cite as: J. Appl. Phys. **131**, 153102 (2022); doi: 10.1063/5.0085955
Submitted: 20 January 2022 · Accepted: 3 April 2022 ·
Published Online: 19 April 2022

S. Khattou,[1,a)] M. Amrani,[1] A. Mouadili,[2] E. H. El Boudouti,[1] A. Talbi,[3] A. Akjouj,[4] and B. Djafari-Rouhani[4]

AFFILIATIONS

[1]LPMR, Département de Physique, Faculté des Sciences, Université Mohammed I, Oujda, Morocco
[2]LMECS, Département de Physique, Faculté des Sciences et Techniques de Mohammedia, Université Hassan II, Casablanca, Morocco
[3]Univ. Lille, CNRS, Centrale Lille, ISEN, Univ. Valenciennes, UMR 8520 -IEMN - LIA LICS/LEMAC, F-59000 Lille, France
[4]IEMN, UMR CNRS 8520, Département de Physique, Université de Lille, 59655 Villeneuve d'Ascq, France

[a)]**Author to whom correspondence should be addressed:** s.khattou@ump.ac.ma

ABSTRACT

We propose the design of three port photonic and plasmonic demultiplexers where filtering toward the two outputs is based on the phenomena of Fano resonances and electromagnetically induced transparency (EIT). We use a Cross-shape resonator in one output and a U-shape resonator composed of two stubs in the other output. We give a theoretical demonstration of the geometrical parameters of both resonators in order to filter one wavelength in one output while leaving the other output unperturbed. These results are confirmed by experimental validation in the radio frequency domain and a numerical simulation in the infrared (IR) domain using plasmonic metal–insulator–metal waveguides. The Cross resonator in the first output can give rise to an EIT resonance, whereas the U-shaped resonator in the second output may exhibit both EIT and Fano resonances depending on the lengths chosen for the stubs. Therefore, different demultiplexing schemes can be proposed such as achieving a Fano resonance in one output and an EIT in the other, or EIT resonances in both outputs. The Fano resonance is obtained by bringing resonance close to transmission zero, whereas the EIT results from the squeezing of resonance between two transmission zeros. When the widths of the resonances tend to zero, they transform to trapped or bound states in the continuum with an infinite lifetime. We show that the crosstalk between the two channels can be reduced to −82 dB and the sensitivity can reach 2390.8 nm/RIU, RIU is the refractive index units. Finally, we highlight the performance of our design as a high sensitive filter and sensor in the IR domain. In this work, the analytical calculations and demonstrations are performed by using Green's function approach, the experimental verifications are realized by means of coaxial cables operating in the radio frequency range and the numerical simulations are obtained using the finite element method via Comsol Multiphysics software.

I. INTRODUCTION

Fano and electromagnetic induced transparency (EIT) resonances were originally discovered in quantum systems and interpreted in terms of the coupling between discrete localized states and a continuum of states.[1,2] An EIT resonance appears as symmetric resonance between two antiresonances (two transmission zeros),[2] whereas a Fano resonance occurs in the transmission spectrum as resonance (transmission maximum) followed by an antiresonance (transmission zero); therefore, it displays an asymmetrical profile shape described by the Fano formula.[1] On the other hand, bound states in the continuum (BICs) have known a great deal of interest, thanks to their interesting characteristics.[3] These states appear as zero-width resonances in the transmission spectra with infinite quality factors. In recent years, these different types of resonances have attracted growing attention because they can provide potential applications in slow light[4] and high-performance nano-sensing.[5–7] These phenomena have been extended to classical systems in different areas such as acoustic slender tube waveguides,[8,9] photonic circuits,[10–12] plasmonic nanostructures,[13–17] and metasurfaces.[18]

Due to their potential applications in communication systems, several works have been devoted during the last two decades to the study of wavelength demultiplexers based on photonic crystals. Wavelength selection in such systems can be realized through different mechanisms such as defect waveguides,[19–21] resonant cavities,[13,14,22,23] superprisms,[24] slot waveguides,[25,26] channel drop filters,[27] ring resonators in photonic crystals,[28–30] and bandstop filters.[31] In designing photonic crystal-based demultiplexers, the most important factors that can define the performance of demultiplexers consists in achieving high transmission efficiency together with a high-quality factor of the resonant wavelengths and reduced crosstalk between the outputs. Recently, Fano and EIT resonances as well as BICs have been used in different three port demultiplexers such as photonic circuits[32,33] and plasmonic nanodevices.[34–36]

In recent papers of our research team,[10,11] Cross and U-shaped resonators have been studied in two port photonic structures to achieve EIT and Fano resonances. We have shown that the Cross structure may exhibit only EIT-type resonance, while the U-shaped resonator can present both EIT and Fano resonances. In plasmonic systems, several works[15,37–40] have used Cross and U-shaped coupled resonators to achieve PIT (the plasmonic analog of electromagnetic induced transparency) and Fano resonances for slow light and sensing applications.[6,7] Recently, photonic and plasmonic demultiplexers operating in radio frequency and infrared domains have been proposed based on either Cross[32,34] or U-shaped[33,36] stubs. In this paper, we give a theoretical demonstration with numerical and experimental validations of both photonic and plasmonic wavelength demultiplexers based on a mixed configuration of Cross and U-shaped resonators with applications for filtering and sensing. The latter demultiplexer consists of one input channel connected to two output channels. The first output channel contains a Cross-shaped structure, whereas the second channel contains an U-shaped resonator (Fig. 1). The main objective of this work consists of deriving analytically all the geometrical lengths in the demultiplexers to realize a complete transmission in one channel without perturbing the other one and vice versa. In contrast to a demultiplexer based only on Cross-shaped resonators[32] where the EIT mechanism is used in both channels, the advantage of the mixed demultiplexer is to allow various possibilities such as using the EIT mechanism in both channels or EIT resonance in one output and Fano resonance in the other. The idea consists of bringing in coincidence the transmission zero associated with resonance in one line with the maximum of the resonance in the other line. In this paper, we use Green's function method[41,42] to make the analytical demonstrations and derivations of the geometrical parameters to obtain the wavelength demultiplexing conditions; then, the theoretical predictions are validated in a setup using coaxial cables operating in the radio frequency range.[43–45] Also, a numerical simulation is given for a plasmonic demultiplexer based on metal–insulator–metal (MIM) waveguides. This design shows a good efficiency for filtering and sensing applications in the infrared domain.

The paper is organized as follows. In Sec. II, we present the application of Green's function formalism[41,42] to deduce the analytical calculations of the reflection and transmission coefficients through the demultiplexer. This section is divided into two subsections. In Subsection II A, we consider the case of EIT resonances in both outputs (EIT–EIT) and give the analytical expressions of the different geometrical parameters to make the demultipexing efficient. In addition, we present some numerical results with an experimental validation in the radio frequency domain using coaxial cables. Subsection II B gives the same results as in Subsection II A but for the EIT–Fano demultiplexing. Section III provides analytical and numerical results of the MIM plasmonic demultiplexer with a discussion about its performance for filtering and sensing applications. Section IV gives the conclusion of this work.

II. THREE PORT PHOTONIC DEMULTIPLEXER BASED ON MIXED STRUCTURE: THEORY

The mixed demultiplexer presented here is composed of one input and two outputs [Fig. 1(a)]. The first output contains a Cross resonator made of two stubs of lengths d_1 and d_2 placed

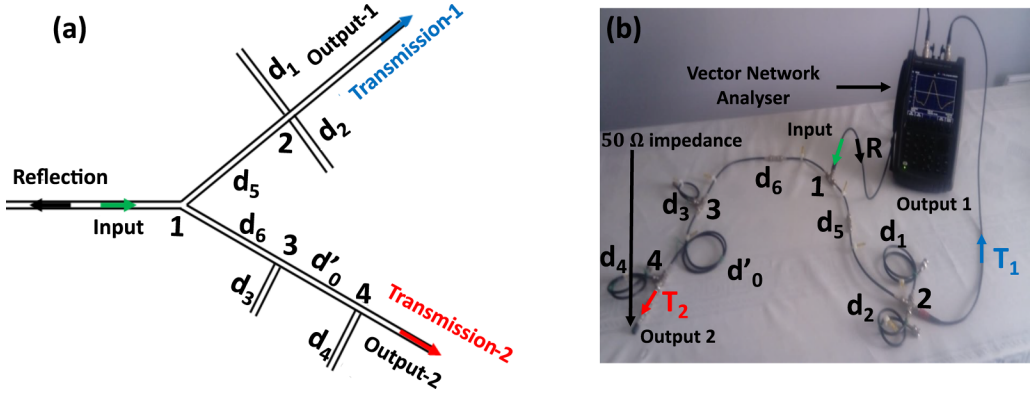

FIG. 1. (a) Schematic illustration of the three port demultiplexer based on U and Cross structures called mixed structure. The first output contains two stubs of lengths d_1 and d_2 placed at the same site {2} at a distance d_5 from the input line {1}. The second output contains two stubs of lengths d_3 and d_4 placed, respectively, at the sites {3} and {4} at a distance d_6 and $d_6 + d'_0$ far from the input line. (b) Experimental setup of the studied demultiplexer using coaxial cables and vector network analyzer working in the radio frequency range. When the measurement is realized along the first output, the second output is terminated by a 50Ω impedance in order to avoid any reflection.

at the same position labeled {2} and connected to the input labeled {1} by the segment of length d_5. The second output contains a U-shaped resonator made of two stubs of lengths d_3 and d_4 placed, respectively, at the sites {3} and {4} at a distance d_6 and $d_6 + d_0'$ from the input line [Fig. 1(a)]. The Cross resonator in the first output may exhibit only EIT resonances, while the U-shaped resonator in the second output may exhibit both Fano and EIT resonances. Therefore, two possibilities of demultiplexing can be achieved such as EIT mechanism in both channels or EIT resonance in one output and Fano resonance in the other output.

The reflection and transmission coefficients through the mixed demultiplexer shown in Fig. 1(a) can be derived from the knowledge of the inverse of Green's function of the entire system [Fig. 1(a)] in the space of interface $M = \{1, 2, 3, 4\}$. This latter can be build from the juxtaposition of the elementary constituents,[41,42] namely,

$$g^{-1}(MM) = -F\begin{pmatrix} \frac{C_5}{S_5} + \frac{C_6}{S_6} - j & -\frac{1}{S_5} & -\frac{1}{S_6} & 0 \\ -\frac{1}{S_5} & \frac{C_5}{S_5} + \frac{S_1}{C_1} + \frac{S_2}{C_2} - j & 0 & 0 \\ -\frac{1}{S_6} & 0 & \frac{C_6}{S_6} + \frac{C_0'}{S_0'} + \frac{S_3}{C_3} & -\frac{1}{S_0'} \\ 0 & 0 & -\frac{1}{S_0'} & \frac{C_0'}{S_0'} + \frac{S_4}{C_4} - j \end{pmatrix}, \tag{1}$$

where $C_i = \cos(kd_i)$, $S_i = \sin(kd_i)$ $(i = 0, 0', 1, 2, 3, 4, 5, 6)$, $F = \frac{\omega}{Z}$, and $j = \sqrt{-1}$. The wave vector of the incident wave is given by $k = \frac{\omega\sqrt{\epsilon_d}}{c}$, where c is the speed of light in vacuum, ω is the pulsation, ϵ_d is the dielectric permittivity of the waveguides, and Z is the impedance of the cables.

The reflection coefficient r in the input and the transmission coefficients in the first and second outputs (t_1 and t_2) can be obtained, respectively, as[41] $r = -1 - 2jFg(1, 1)$, $t_1 = 2jFg(1, 2)$, and $t_2 = 2jFg(1, 4)$. The elements $g(1, 1)$, $g(1, 2)$, and $g(1, 4)$ are obtained by inverting the 4×4 matrix in Eq. (1). These expressions are cumbersome, that is why we shall avoid giving them here; however, we shall provide below the necessary conditions that should be fulfilled by the waveguide lengths to achieve an efficient demultiplexing.

A. Three port photonic demultiplexer: EIT–EIT resonances

Let us start with the case where the two resonances are of EIT-type on both outputs. In order to obtain a full transmission in the first output (i.e., $T_1 = 1$), both T_2 and R should cancel at the same frequency (i.e., $T_2 = R = 0$). For this purpose, the following analytical expressions should be satisfied: $C_3 = 0$ (or $C_4 = 0$), $C_6 = 0$, and $\sin(kd_0) = 0$, where $d_0 = d_1 + d_2$. Likewise, a complete transmission in the second channel (i.e., $T_2 = 1$, $T_1 = R = 0$) requires $C_1 = 0$ (or $C_2 = 0$), $C_5 = 0$, and $\sin(k(d_0 + \delta)) = 0$. Therefore, the lengths of the segments and stubs should verify the following conditions:

$$d_1 = \frac{d_0}{2} - \frac{\delta}{2}, \tag{2}$$

$$d_2 = d_5 = \frac{d_0}{2} + \frac{\delta}{2}, \tag{3}$$

$$d_3 = d_6 = \frac{d_0}{2}, \tag{4}$$

$$d_4 = \frac{d_0}{2} + \delta, \tag{5}$$

$$d_0' = d_0 + \delta, \tag{6}$$

where $\delta = d_2 - d_1$ is the detuning between the two stubs of lengths d_1 and d_2.

Figure 2 shows the reflection coefficient magnitude (R) along the input and the transmission coefficient magnitudes (T_1 and T_2) along the two outputs of the demultiplexer [Fig. 1(a)] vs the dimensionless frequency $\Omega = \frac{\omega d_0\sqrt{\epsilon_d}}{c}$ for three values of the detuning δ. The waveguides are supposed lossless. The transmission through the first output is plotted in the blue line, the transmission through the second output is shown in the red line, and the reflection at the input of the demultiplexer is given by the black line. The curves show that the transmission in one line is total for a given Ω when the transmission in the other output and the reflection at the input of the demultiplexer vanish. The filtered resonances are squeezed between two transmission zeros, this is a characteristic of EIT resonances. We also notice that the position of the EIT resonance in the first output (T_1) remains constant at the same dimensionless frequency $\Omega = \pi$ since d_0 is fixed at $d_0 = 1$, while the position of the EIT resonance in the second output changes as δ changes. The width of the resonances depends on δ, it increases when δ increases, giving rise to a decreasing in the quality factor as a function of δ. Also, the quality factor of the first EIT resonance (in blue) remains almost constant when δ changes sign (Q = 8.65), however, the quality factor of the second EIT resonance (in red) takes the value 23.40 for $\delta = 0.2d_0$ [Fig. 2(a)] and 10.85 for $\delta = -0.2d_0$ [Fig. 2(c)]. In addition, for $\delta = 0.2$, the EIT resonance in the second output appears below the EIT resonance in the first output [Fig. 2(a)], whereas for $\delta = -0.2d_0$ the second EIT resonance reappears above the first resonance [Fig. 2(c)]. Moreover, one can remark that the EIT resonance in the second output (in red) in Figs. 2(a) and 2(c) is not symmetric vs δ. This is due to the non-symmetric dependence of the lengths of the

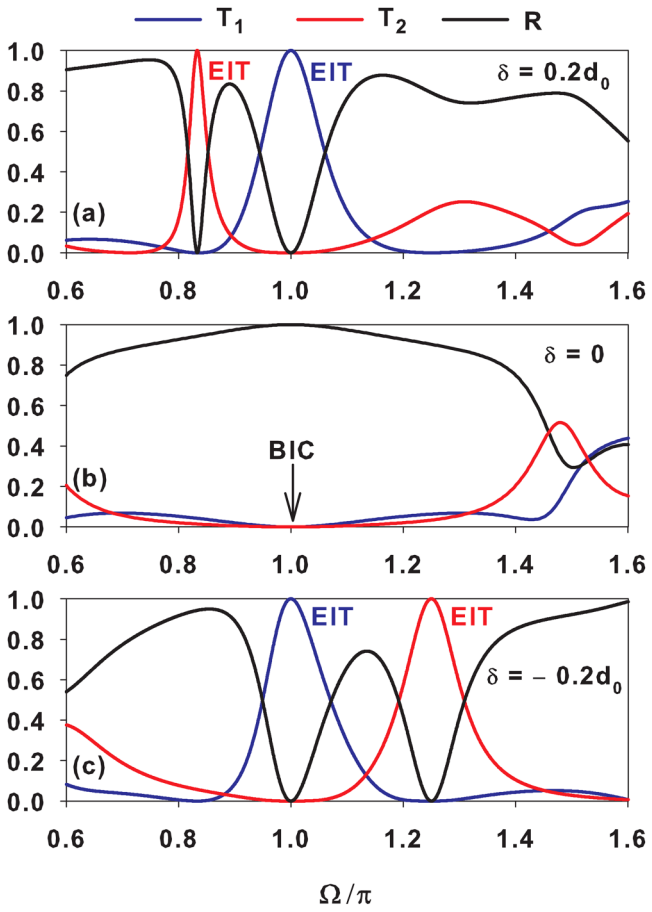

FIG. 2. Transmission coefficient magnitudes in the first output (blue lines), second output (red lines) and the reflection magnitude at the input (black lines) of the mixed demultiplexer vs the dimensionless frequency Ω/π for (a) $\delta = 0.2d_0$, (b) $\delta = 0$, and (c) $\delta = -0.2d_0$, where $d_0 = d_1 + d_2$ is considered fixed. The other lengths of the waveguides are chosen according to Eqs. (2)–(6).

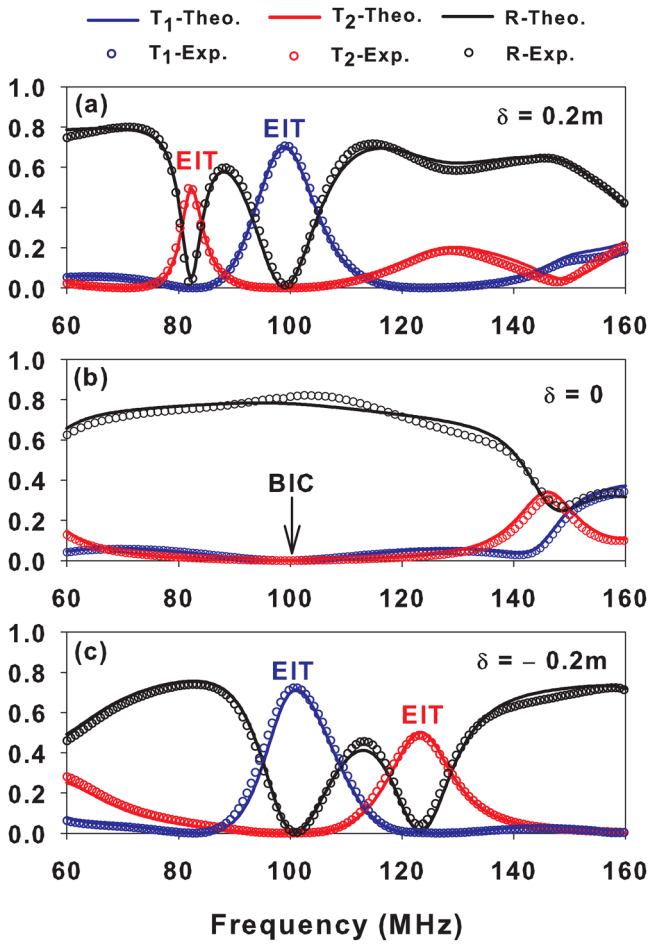

FIG. 3. Theoretical reflection and transmission coefficient magnitudes (continuous lines) as a function of the frequency along the outputs 1 (blue curves) and 2 (red curves) of the demultiplexer for (a) $\delta = 0.2$ m, (b) $\delta = 0$, and (c) $\delta = -0.2$ m. Black curves represent the reflection coefficient magnitude. Experimental data are plotted by open circles.

structure as a function of δ [see Eqs. (2)–(6)]. The sign of δ affects considerably the width of the resonances on both outputs. In the particular case $\delta = 0$, both EIT resonances fall at $\Omega = \pi$ giving rise to a BIC (i.e., zero-width resonance) as it is shown in Fig. 2(b). Therefore, the quality factor of the BIC mode tends to infinity for the lossless system.

Figure 3 displays an experimental validation of the theoretical results discussed in Fig. 2 for three values of δ. The coaxial cables used in the realization of the structure described in Fig. 1(a) are chosen such that the lengths of the cables satisfy Eqs. (2)–(6). The experiment is performed using standard coaxial cables RG-58/U of different lengths with the same characteristic impedance $Z = 50\Omega$ [Fig. 1(b)]. The segments of coaxial cables were connected by standard BNC T-connectors. The cables were filled with polyethylene ($\varepsilon' = 2.3$), corresponding to a nominal propagation speed of $0.66c$. The boundary conditions at the upper ends of the stubs are H = 0 (i.e., vanishing magnetic field). The attenuation in the coaxial cables was simulated by introducing a complex dielectric permittivity $\varepsilon = \varepsilon' + j\varepsilon''$. The attenuation coefficient α'' can be expressed as $\alpha'' = \varepsilon''\omega/c\sqrt{\varepsilon'}$. On the other hand, the attenuation specification data supplied by the manufacturer of the coaxial cables based on energy decreasing of the waves along the cables in the frequency range of 10–200 MHz can be approximately fitted with the expression $\ln(\alpha'') = \gamma + \beta \ln(\omega)$, where γ and β are two constants. From this fitting procedure, a useful expression as a function of frequency can be obtained under the form $\varepsilon'' = \left(\frac{f}{f_0}\right)^{-0.5}$, where the frequency f is expressed in Hz and $f_0 = 9200$ Hz. The resolution of amplitude and phase measurement are around 0.5 mV and 0.01, respectively, using an intermediate frequency (IF) filter bandwidth of 1 KHz. The dynamic range is around 100 dB. The noise of the VNA at GHz frequency is too small (0.01 mV rms) and is

drastically reduced by the IF filter. The measured S-parameters are accurate and reliable, and the error is less than 0.2%. Figure 3 shows a good agreement between the theoretical results (solid lines) and the experimental results (open circles). The curves show that the filtered resonances in the two outputs are of EIT type. Due to the attenuation in the cables, the transmission and reflection spectra do not exceed 80%. However, the transmission exhibits a maximum value in the first output when both the transmission in the second output and the reflection in the input get closer to zero and vice versa. Also, one can notice that the quality factor of the first EIT resonance (in blue) is almost the same (Q = 8.36) when δ changes the sign, whereas for the second EIT resonance (in red), the quality factor becomes 17.29 for $\delta = 0.2$ m [Fig. 3(a)] and 8.87 for $\delta = -0.2$ m [Fig. 3(c)]. These values are slightly lower than those obtained in Fig. 2 in the absence of loss. For the BIC ($\delta = 0$), the width of the resonance in the transmission is ill-defined [Fig. 3(b)] and so the quality factor of the resonance. In addition, one of the most important parameter that characterizes the performance of the demultiplexer is the crosstalk. This quantity is defined as the quotient of the transmission power (in dB) of the desired output and the other output.[29] In Fig. 3(a), the crosstalk rate between the two outputs for the frequency 96.36 MHz is about −29.18 dB. This rate becomes about −23.44 dB for the frequency 122.86 MHz. The results in Fig. 3 show a clear experimental validation of the theoretical results in Fig. 2.

B. Three port photonic demultiplexer: EIT–Fano resonances

In the case where the two stubs of lengths d_3 and d_4 are taken identical and their lengths slightly different from half of the length of the segment, which separates them (i.e., $d_3 = d_4 \neq \frac{d_0'}{2}$), the U-shaped structure presents Fano-type resonances.[11] The Cross structure connected to the other output exhibits EIT resonances. Now, by appropriately choosing the different lengths of the waveguides which constitute the mixed demultiplexer [Fig. 1(a)], it is possible to achieve mixed filtering where one can obtain a Fano resonance on the second output and EIT resonance on the first output. Indeed, in order to obtain a complete filtering in the first output with transmission and reflection zeros in the second output and the input, one should satisfy $C_3 = 0$ (or $C_4 = 0$), $C_6 = 0$, and $\sin(kd_0) = 0$. Similarly, an efficient transfer in the second output requires $C_1 = 0$ (or $C_2 = 0$), $C_5 = 0$, and $\sin(k(d_0 + \delta)) = 0$ for the second output. Therefore, the lengths of the segments and stubs must satisfy the following equations:

$$d_1 = \frac{d_0}{2} - \frac{\delta}{2}, \tag{7}$$

$$d_2 = d_5 = \frac{d_0}{2} + \frac{\delta}{2}, \tag{8}$$

$$d_3 = d_4 = d_6 = \frac{d_0}{2}, \tag{9}$$

$$d_0' = d_0 + 2\delta, \tag{10}$$

where $\delta = d_2 - d_1$.

Figure 4 shows the transmissions magnitudes (T_1 and T_2) and the reflection magnitude (R) spectra as a function of the dimensionless frequency Ω for three values of δ. The lengths of the different stubs and segments are chosen according to Eqs. (7)–(10). One can see that the resonance is of EIT type in output 1 (blue curves) and of Fano type in output 2 (red curves). Figure 4 shows that the EIT resonance in the first output occurs at the same reduced frequency $\Omega = \pi$ for different values of δ since d_0 is fixed. On the other hand, the position of the Fano resonance in the second output varies as a function of δ. Indeed, for $\delta = 0.2d_0$ [Fig. 4(a)] the Fano resonance appears at the left side of the EIT resonance. Whereas, for $\delta = -0.2d_0$ [Fig. 4(c)] the Fano resonance occurs at the right side of the EIT resonance. In addition, the

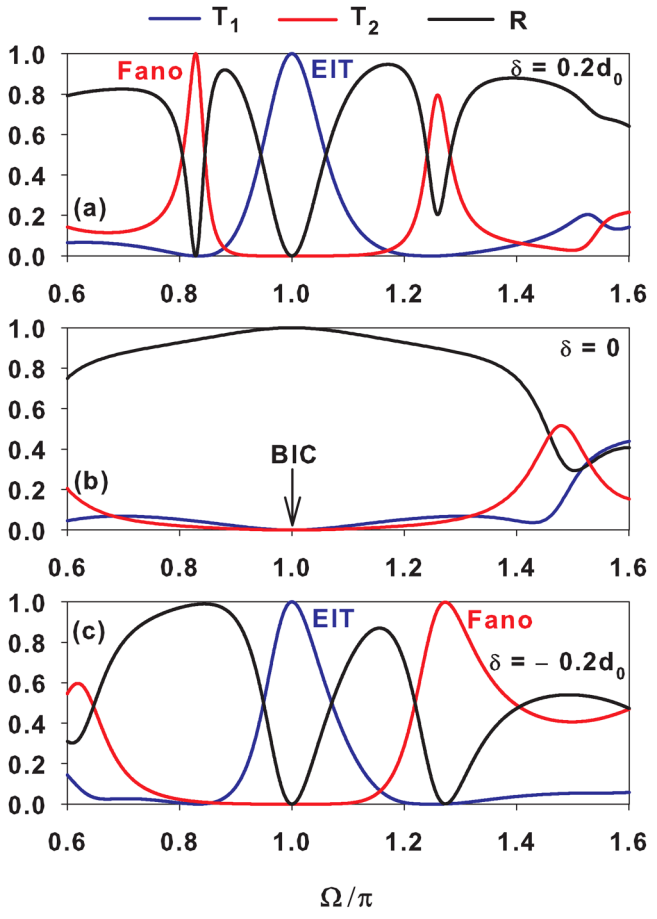

FIG. 4. Transmission coefficient magnitudes in the first output (blue lines), second output (red lines), and the reflection magnitude at the input (black lines) of the mixed demultiplexer vs Ω/π for (a) $\delta = 0.2d_0$, (b) $\delta = 0$, and (c) $\delta = -0.2d_0$. The lengths of the waveguides are chosen according to Eqs. (7)–(10).

width of both resonances changes when the sign of δ changes. In Fig. 4(a), we also notice the existence of another Fano resonance at the right side of the EIT resonance around $\Omega = 1.26$. This latter does not reach unity since Eqs. (7)–(10) are not fulfilled at this frequency. For $\delta = 0$ [Fig. 4(b)], both resonances fall at $\Omega = \pi$ and appear with zero width, giving rise to BICs. These modes correspond to stationary waves in the Cross and U-shaped stubs on both outputs and do not interact with the semi-infinite wires (continuum states) surrounding them.

Experimental validation of the previous theoretical results for three values of δ (Fig. 4) is presented in Fig. 5. The solid lines present the theoretical results, whereas open circles show the experimental measurements. Figure 5 shows that in channel 1, we have an EIT-type resonance, while in channel 2, we have a Fano-type resonance. In addition, the amplitudes of the resonances in the transmission spectra do not reach unity because of the loss effect in the cables. The transmission is maximum in output 1 when both the transmission in the other output and the reflection in the input get close to zero. As mentioned before, the quality factor of the first EIT resonance (in blue) is not much affected by the sign of δ and remains almost constant (Q=8.36) when δ changes the sign, whereas the Fano resonance (in red) exhibits high-quality factor Q = 12.90 for $\delta = 0.2d_0$ than for $\delta = -0.2d_0$, where Q = 6.84. Therefore, its amplitude is more affected by the loss effect in the cables. In Fig. 5(a), the crosstalk rate between the two outputs for the frequency 82.51 MHz is about −21.44 dB. This rate becomes about −73.04 dB for the frequency 97.40 MHz. We note that the proposed three port demultiplexer may present lower crosstalk values in comparison with those reported in the literature,[46,47] where the demultiplexing is based on Lorentzian resonances with symmetric line shapes instead of Fano or EIT resonances. The experimental results in Fig. 5 show a good agreement with the theoretical one in Fig. 4. Let us mention here that the EIT and Fano resonances shown in Figs. 2–5 are obtained for any value of $\delta \neq 0$. However, it is better to not exceed $\delta = 0.35d_0$ as the EIT resonance in the first output deteriorates and loses its symmetric character (i.e., resonance squeezed between two transmission zeros), however, the Fano resonance keeps its Fano shape (i.e., resonance followed by transmission zero) even though δ is greater than $\delta = 0.35d_0$.

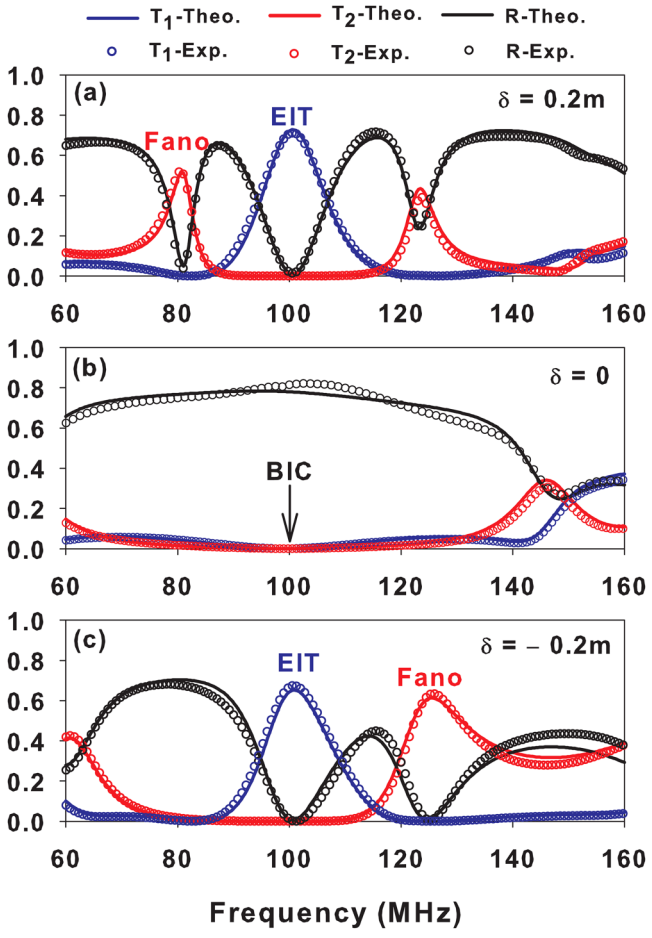

FIG. 5. Theoretical reflection and transmission coefficient magnitudes (continuous lines) as a function of the frequency along the outputs 1 (blue curves) and 2 (red curves) of the demultiplexer for (a) $\delta = 0.2$ m, (b) $\delta = 0$, and (c) $\delta = -0.2$ m. Black curves represent the reflection coefficient magnitude. Experimental data are plotted by open circles.

III. THREE PORT PLASMONIC DEMULTIPLEXER: ANALYICAL AND NUMERICAL RESULTS IN THE INFRARED DOMAIN

The wavelength demultiplexing presented in Sec. II can be applied to a plasmonic demultiplexer based on MIM nanowaveguides operating in the infrared domain. The two-dimensional MIM plasmonic demultiplexer based on the mixed configuration of Cross and U-shaped resonators is sketched in Fig. 6(a). The width of the bus waveguide and stubs are set to be equal w = 50 nm, which is much smaller than the surface plasmon polariton (SPP) wavelength ($w \ll \lambda_{sp}$) in order to ensure only the propagation of the fundamental transverse magnetic (TM_0) mode excitation. The stubs and bus waveguide are filled with air, whereas the surrounding metal is made of silver with a frequency-dependent complex permittivity ε_m described by the Drude model[48,49]

$$\varepsilon_m = \varepsilon_\infty - \frac{\omega_p^2}{\omega^2 + j\gamma\omega}, \tag{11}$$

where $\varepsilon_\infty = 3.7$ is the dielectric constant at the infinite frequency, $\omega_p = 1.38 \times 10^{16}$ rad/s denote the bulk plasma frequency, $\gamma = 2.634 \times 10^{13}$ rad/s is the electron collision frequency, and ω shows the angular frequency of the incident light. These values fit well the experimental data of silver in the visible and infrared range.[50]

Two important key physical quantities that describe the behaviors of SPP propagation within the demultiplexer device are the wave vector k_{sp} and the impedance Z of the MIM waveguide. These two quantities are dependent on material parameters and magnitude of the system. Then, the SPP propagation wave vector

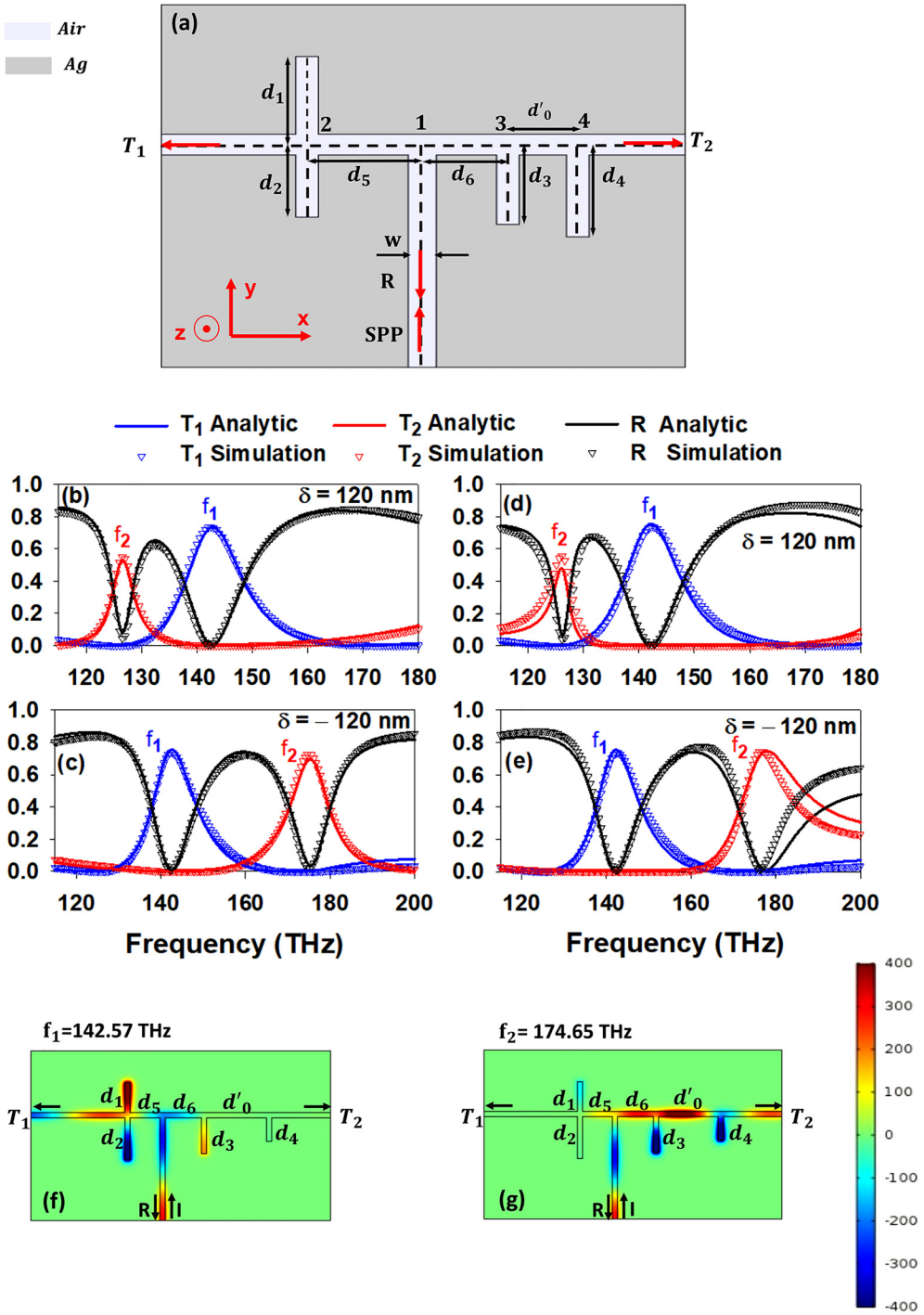

FIG. 6. (a) Three port MIM plasmonic demultiplexer based on mixed configuration of Cross and U-shaped resonators. (b) and (c) Transmission along the first output (blue curves) and second output (red curves), as well as the reflection along the input (black curves) vs frequency for $\delta = 120$ nm and $\delta = -120$ nm, respectively, in the case of PIT–PIT demultiplexing. Solid lines represent analytical results, whereas open triangles give the numerical simulations. (d) and (e) Same as in (b) and (c) but for PIT–Fano demultiplexing. (f) and (g) H_z field map of the two filtered PIT resonances at $f_1 = 142.57$ THz and $f_2 = 174.65$ THz, respectively, for $\delta = -120$ nm in (c). I, R, T_1, and T_2 indicate the incident, reflected and transmitted waves along the input and the two outputs.

k_{sp} of the fundamental propagating TM_0 mode in the MIM waveguide is given by[48]

$$k_{sp} = k_0\sqrt{\varepsilon_d - \frac{2\varepsilon_d\sqrt{\varepsilon_d - \varepsilon_m}}{\varepsilon_m k_0 \mathrm{w}}}, \tag{12}$$

where $k_0 = \frac{\omega}{c}$ is the wave vector in vacuum. ε_d and ε_m denote the dielectric constants of the dielectric and the metal, respectively. The other interesting quantity that characterizes the MIM waveguide is the impedance Z, which is given by[48]

$$Z = \frac{k_{sp}\mathrm{w}}{\varepsilon_d\omega}. \tag{13}$$

The structure depicted in Fig. 6(a) is a 2D system in the (x,y) plane and infinite in the z-direction. This design is the most used in MIM waveguides simulations as it is less time consuming. However, for practical processing, the MIM waveguides are 3D as they present a finite height h along the z-direction and they are deposited on SiO_2 substrate. The finite depth of the system and the surrounding media introduce a significant effect on loss in the system. Nevertheless, it was shown that above a certain height ($h = 50$ nm), 2D and 3D models provide almost similar results,[51–53] in particular, as concerns the positions of the resonant modes in the transmission spectra,[51] even their shapes and widths can be affected.

In a realistic structure, the dielectric waveguide is fully immersed in a metal [Fig. 6(a)]. This is exactly the model which we have studied in the finite element simulation approach. However, in the analytical approach, the MIM waveguide (including the horizontal part and the stubs) is replaced by a unique waveguide characterized by the wavevector k_{sp} [Eq. (12)] and the impedance Z [Eq. (13)]. Therefore, it becomes necessary to define a boundary condition at the end of the stubs. Since the top of the stubs is in contact with the silver metal, we apply a boundary condition meaning that the stub is connected to a semi-infinite metal waveguide of width w and characterized by the impedance

$$Z_m = \frac{k_m\mathrm{w}}{\varepsilon_m\omega}, \tag{14}$$

where $k_m = k_0\sqrt{\varepsilon_m}$.

The calculation of transmission and reflection coefficients for the plasmonic demultiplexer [Fig. 6(a)] is similar to the one of the photonic devices presented in Sec. II, just we need to replace in Eq. (1), k by k_{sp} [Eq. (12)] and F by ωZ. Also, it is necessary to take into account the semi-infinite metal at the end of the coupled stubs. This can be achieved by replacing in Eq. (1) the quantity $\frac{-S_i}{C_i}$ by $A_i = \frac{ZS_i + jZ_mC_i}{ZC_i - jZ_mS_i}$ $(i = 1, 2, 3, 4)$, where $C_i = \cos(k_{sp}d_i)$ and $S_i = \sin(k_{sp}d_i)$.

Figures 6(b) and 6(c) give the transmission spectra through the first (blue curves) and second (red curves) outputs and the reflection (black curves) along the input as a function of frequency for $\delta = 120$ nm and $\delta = -120$ nm, respectively. d_0 is fixed at $d_0 = 700$ nm and the detuning δ between the two stubs d_1 and d_2 is chosen variable. The analytical results (solid lines) obtained by Green's function method are confirmed by numerical simulations based on 2D finite element method using Comsol Multiphysics software. Both results show a good agreement. The results in Figs. 6(b) and 6(c) are plotted according to PIT–PIT conditions [Eqs. (2)–(6)]; therefore, the two resonances are both of PIT type. In addition, one can see that the PIT resonance in the first output appears at the same frequency $f_1 = 142.57$ THz since d_0 is fixed at $d_0 = 700$ nm with a transmission efficiency 73%, whereas the second PIT resonance falls at two different positions as δ changes: the PIT resonance in the second output appears at $f_2 = 126.52$ THz with a transmission efficiency about 54% for $\delta = 120$ nm [Fig. 6(b)] and at $f_2 = 174.65$ THz with a transmission efficiency about 72% for $\delta = -120$ nm [Fig. 6(c)]. One can see here also that the maximum of the transmission in one output coincides well with the zeros of the transmission in the other output and the reflection in the input in accordance with the analytical calculations developed in Sec. II. In addition, the best crosstalk for the PIT–PIT demultiplexing can reach -45.36 dB at the frequency 142.57 THz for $\delta = -120$ nm in Fig. 6(c). Similarly, Figs. 6(d) and 6(e) show the results for the PIT–Fano demultiplexing for $\delta = 120$ nm and $\delta = -120$ nm, respectively. These results are plotted using the conditions of PIT–Fano demultiplexing [Eqs. (7)–(10)]. The first resonance which appears at $f_1 = 142.57$ THz is of PIT type, whereas the second resonance is of Fano type. The position of the latter resonance depends on δ. For $\delta = 120$ nm, the resonance appears at $f_2 = 126.11$ THz with a transmission efficiency about 55%, whereas the second resonance for $\delta = -120$ nm occurs at $f_2 = 176.65$ THz with a transmission efficiency about 74%. The magnitudes of the transmission and reflection coefficients in Figs. 6(b)–6(e) do not reach unity due to the intrinsic metal loss. In addition, the crosstalk rates can achieve lower values about -80.70 dB for the PIT resonance in Fig. 6(d) and about -82.36 dB for the PIT resonance in Fig. 6(e). We note that our proposed plasmonic demultiplexer may present best crosstalk values than the photonic demultiplexer discussed in Sec. II and in comparison with other previous works in the literature for three port plasmonic demultiplexers.[54,55] These results are grouped in Table I. Let us mention that for a lossless system, the transmission can reach unity in one output ($T = 1$) with a transmission zero $T = 0$) in the other output, and, therefore, the crosstalk in this case goes to infinity.

TABLE I. Comparison of crosstalk with previous works and for different configurations.

Structure		Crosstalk (dB)
Photonic demultiplexer	EIT–EIT	−29.18
	EIT–Fano	−73.04
Plasmonic demultiplexer	PIT–PIT	−45.36
	PIT–Fano	−82.36
Ref. 46		−18.35
Ref. 47		−17.63
Ref. 54		−28
Ref. 55		−30

However, for lossy systems as it is the case here the crosstalk presents finite values.

In order to study the spatial localization of the filtered resonances along the two outputs, we plotted in Figs. 6(f) and 6(g) the H_z field map of the two filtered PIT resonances at $f_1 = 142.57$ THz and $f_2 = 174.65$ THz, respectively, for $\delta = -120$ nm in Fig. 6(c). From Fig. 6(f), one can see that the SPP wave at $f_1 = 142.57$ THz propagates along the first output through the excitation of the modes of the stubs of lengths d_1 and d_2 of the Cross-shape resonator, whereas it is stopped along the second output due to the excitation of the stationary mode of the stub of length d_3 of the U-shaped resonator. On the other hand, the H_z filed map in Fig. 6(g) shows that the SPP wave at $f_2 = 174.65$ THz is transferred along the second output through the excitation of the mode of the stubs of lengths d_3 and d_4 as well as the waveguide d_0' that formed the U-shaped resonator, while it is completely stopped along the first output by the stub of length d_1 through the excitation of its stationary mode.

In all the previous results in Fig. 6, the waveguide was filled with air. Thus, in order to investigate the performance of the proposed device as filter and sensor, we have changed the refractive index n of the waveguide from 1 to 1.25 with a step of 0.05 for a fixed $\delta = 120$ nm and for different filtered resonances such as PIT resonance in output 1 [Fig. 7(a)], PIT resonance in output 2 [Fig. 7(b)], and Fano resonance in output 2 [Fig. 7(c)]. In these figures, the parameters in the first output (Cross structure) give only PIT resonances, whereas the parameters in the second output (U structure) can show either PIT or Fano resonances. Even though the structures in the second output are different, they do not affect those in the first output. One can notice that when n increases from 1 to 1.25 the resonances shift to lower frequencies (higher wavelengths), also their amplitudes decrease. Figure 7(d) presents the variation of the resonance frequency (or wavelength) as a function of n. This figure shows that there is a linear relationship between n and the resonance frequency (or wavelength).

One of the most important parameters that characterize the performance of plasmonic sensors and filters is the wavelength sensitivity. The sensitivity of a filter/sensor is defined as the ratio between the shift of the resonance wavelength $\Delta\lambda$ and the shift in the refractive index Δn, namely,

$$S = \frac{\Delta\lambda}{\Delta n}. \tag{15}$$

In Table II, we give a comparison of the sensitivity values (in nm/RIU) of the proposed device in both outputs with other plasmonic sensors based on MIM coupled waveguides of recent research in the literature.[56,57] In our case, the sensitivity is given for

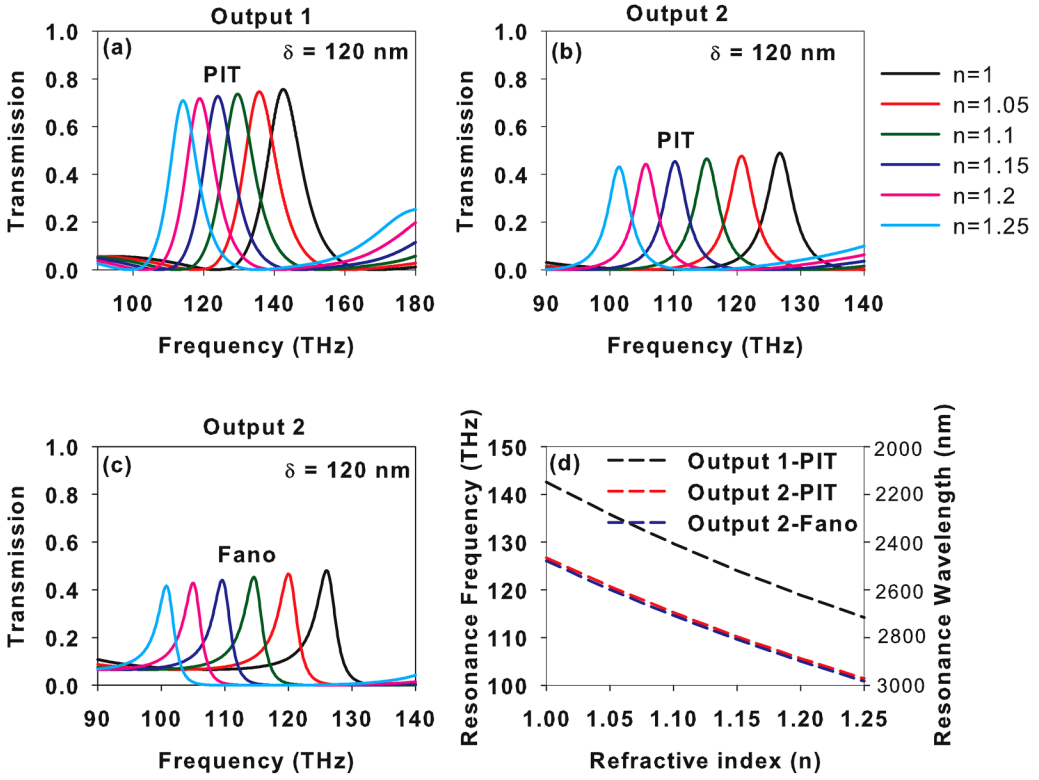

FIG. 7. Transmission magnitude spectra vs the frequency (in THz) along both outputs for different refractive index values n of the waveguide for (a) PIT resonance in output 1, (b) PIT resonance in output 2, (c) Fano resonance in output 2, and (d) resonance frequency (wavelength) vs the refractive index n for different cases in (a)–(c).

TABLE II. Comparison of the sensitivity with previous works and for different configurations.

Structure	Sensitivity (nm/RIU)
This work: PIT-output 1	2101.4
This work: PIT-output 2	2390.8
This work: Fano-output 2	2388.2
Ref. 56	1217
Ref. 57	793.3

different configurations such as PIT resonance in output 1, PIT resonance in output 2, and Fano resonance in output 2. One can notice that the U-shaped resonator in the second output represents very high sensitivity values in comparison with the Cross-shaped resonator in the first output. In addition, the proposed demultiplexer shows a good sensitivity in comparison with other previous works in the literature.[56,57]

IV. CONCLUSION

We presented a theoretical, numerical, and experimental investigation of an efficient three port demultiplexer where the two output channels contain a mixture of detuned stubs. The first channel of our proposed demultiplexer contains a Cross resonator, whereas the second output contains a U-shaped resonator. Due to this mixed combination, different possibilities of demultiplexing can be obtained such as EIT–EIT or EIT–Fano resonances. We derived analytically the closed form expressions for the different lengths of the stubs involved in the structure and demonstrated an efficient selective transfer of one wavelength in one output channel while leaving the second channel unperturbed and vice versa. The various possibilities of wave filtering in the mixed structure are discussed. The analytical demonstrations obtained by means of Green's function method are confirmed by an experimental validation in the radio frequency domain using coaxial cables. In addition, we have shown that our analytical results can be transposed to the infrared domain using a plasmonic demultiplexer based on nanoscale MIM waveguides. The analytical results are confirmed by the finite element calculation based on Comsol Multiphysics software. In the proposed design, the crosstalk quotient between the two output channels can be reduced to below −82 dB and the sensitivity can reach 2390.8 nm/RIU. Therefore, the proposed three port demultiplexer shows good performance for filtering and sensing applications.

ACKNOWLEDGMENTS

The work of S. Khattou and M. Amrani has been supported by the National Center of Scientific and Technical Research (CNRST) under the Excellence Research Scholarship.

AUTHOR DECLARATIONS

Conflict of Interest

The authors have no conflicts to disclose.

DATA AVAILABILITY

The data that support the findings of this study are available from the corresponding author upon reasonable request.

REFERENCES

[1]U. Fano, "Effects of configuration interaction on intensities and phase shifts," Phys. Rev. **124**, 1866 (1961).
[2]K. J. Boller, A. Imamoglu, and S. E. Harris, "Observation of electromagnetically induced transparency," Phys. Rev. Lett. **66**, 2593 (1991).
[3]C. W. Hsu, B. Zhen, A. D. Stone, J. D. Joannopoulos, and M. Solvacic, "Bound states in the continuum," Nat. Rev. Mater. **1**, 16048 (2016).
[4]L. V. Hau, S. E. Harris, Z. Dutton, and C. H. Behroozi, "Light speed reduction to 17 metres per second in an ultracold atomic gas," Nature **397**, 594 (1999).
[5]S. Wang, T. Zhao, S. Yu, and W. Ma, "High-performance nano-sensing and slow-light applications based on tunable multiple Fano resonances and EIT-like effects in coupled plasmonic resonator system," IEEE Access **8**, 40599 (2020).
[6]R. Adhikari, D. Chauhan, G. T. Mola and R. P. Dwivedi, "A review of the current state-of-the-art in Fano resonance-based plasmonic metal-insulator-metal waveguides for sensing applications," Opto-Electron. Rev. **29**, 148 (2021).
[7]M. Soler and L. M. Lechuga, "Principles, technologies, and applications of plasmonic biosensors," J. Appl. Phys. **129**, 111102 (2021).
[8]A. Mouadili, E. H. El Boudouti, and B. Djafari-Rouhani, "Acoustic demultiplexer based on Fano and induced transparency resonances in slender tubes," Eur. Phys. J. Appl. Phys. **90**, 10902 (2020).
[9]T. Gu, Y. Cheng, Z. Wen, E. H. El Boudouti, Y. Jin, Y. Li, and B. Djafari-Rouhani, "Induced transparency based subwavelength acoustic demultiplexers," J. Phys. D: Appl. Phys. **54**, 175301 (2021).
[10]A. Mouadili, E. H. El Boudouti, A. Soltani, A. Talbi, B. Djafari-Rouhani, A. Akjouj, and K. Haddadi, "Electromagnetically induced absorption in detuned stub waveguides: A simple analytical and experimental model," J. Phys.: Condens. Matter **26**, 505901 (2014).
[11]A. Mouadili, E. H. El Boudouti, A. Soltani, A. Talbi, A. Akjouj, and B. Djafari-Rouhani, "Theoretical and experimental evidence of Fano-like resonances in simple monomode photonic circuits," J. Appl. Phys. **113**, 164101 (2013).
[12]N. Caselli, F. Intonti, F. La China, F. Biccari, F. Riboli, A. Gerardino, L. Li, E. H. Linfield, F. Pagliano, A. Fiore, and M. Gurioli, "Generalized Fano lineshapes reveal exceptional points in photonic molecules," Nat. Commun. **9**, 396 (2018).
[13]J. Chen, Z. Li, J. Li, and Q. Gong, "Compact and high-resolution plasmonic wavelength demultiplexers based on Fano interference," Opt. Express **19**, 9976–9985 (2011).
[14]Z. Chen, R. Hu, L. Cui, L. Yu, L. Wang, and J. Xiao, "Plasmonic wavelength demultiplexers based on tunable Fano resonance in coupled-resonator systems," Opt. Commun. **320**, 6 (2014).
[15]S. Paul and M. Ray, "Nonlinearity modulation based multiple Fano resonance and multi-spectral switching in a nanoplasmonic waveguide-coupled cavity system," J. Appl. Phys. **124**, 193104 (2018).
[16]S. Simoncelli, Y. Li, E. Cortes, and S. A. Maier, "Imaging plasmon hybridization of Fano resonances via hot-electron-mediated absorption mapping," Nano Lett. **18**, 3400 (2018).
[17]T. Huang, S. Zeng, X. Zhao, Z. Cheng, and P. P. Shum, "Fano resonance enhanced surface plasmon resonance sensors operating in near-infrared," Photonics **5**, 23 (2018).
[18]S. Jamilana, G. Semouchkin, and E. Semouchkina, "Analog of electromagnetically induced transparency in metasurfaces composed of identical dielectric disks," J. Appl. Phys. **129**, 063101 (2021).
[19]Y. Pennec, M. Beaugeois, B. Djafari-Rouhani, R. Sainidou, A. Akjouj, J. O. Vasseur, L. Dobrzynski, E. H. El Boudouti, J.-P. Vilcot, M. Bouazaoui, and J.-P. Vigneron, Photonics Nanostructures: Fundam. Appl. **6**, 26–31 (2008).

[20]Y. Li, H. Jiang, L. He, H. Li, Y. Zhang, and H. Chen, "Multichanneled filter based on a branchy defect in microstrip photonic crystal," Appl. Phys. Lett. **88**, 081106 (2006).
[21]C. Jin, S. Han, X. Meng, B. Cheng, and D. Zhang, "Demultiplexer using directly resonant tunneling between point defects and waveguides in a photonic crystal," J. Appl. Phys. **91**, 4771 (2002).
[22]A. A. Faghani and E. Yaghoubi, "Triple-channel glasses-shape nanoplasmonic demultiplexer based on multi nanodisk resonators in MIM waveguide," Optik **237**, 166697 (2021).
[23]S. M. Mousavizadeh, M. Soroosh, and F. Mehdizadeh, "Photonic crystal-based demultiplexers using defective resonant cavity," Optoelectron. Adv. Mater. Rapid Commun. **9**, 28 (2015).
[24]A. Khorshidahmad and A. G. Kirk, "Composite superprism photonic crystal demultiplexer: Analysis and design," Opt. Express **18**, 20518 (2010).
[25]M. Gindi, A. Melamed, and D. Malka, "A four green-light demultiplexer using a multi gallium nitride slot-waveguide structure," Photonics Nanostructures: Fundam. Appl. **42**, 100855 (2020).
[26]T. Shoresh, N. Katanov, and D. Malka, "1 × 4 MMI visible light wavelength demultiplexer based on a GaN slot-waveguide structure," Photonics Nanostructures: Fundam. Appl. **30**, 45–49 (2018).
[27]H. Lu, X. Liu, Y. Gong, D. Mao, and L. Wang, "Enhancement of transmission efficiency of nanoplasmonic wavelength demultiplexer based on channel drop filters and reflection nanocavities," Opt. Express **19**, 12885 (2011).
[28]T. Nurmohammadi, K. Abbasian, and R. Yadipour, "A proposal for a demultiplexer based on plasmonic metal insulator metal waveguide-coupled ring resonator operating in near-infrared spectrum," Optik **142**, 550 (2017).
[29]G. Delphi, S. Olyaee, M. Seifouri, and A. Mohebzadeh Bahabady, "Design of low cross-talk and high-quality-factor 2-channel and 4-channel optical demultiplexers based on photonic crystal nano-ring resonator," Photonic Netw. Commun. **38**, 250 (2019).
[30]H. Liu, Y. Gao, B. Zhu, G. Ren, and S. Jian, "A T-shaped high resolution plasmonic demultiplexer based on perturbations of two nanoresonators," Opt. Commun. **334**, 164 (2015).
[31]Z. Wei, X. Zhang, N. Zhong, X. Tan, X. Li, Y. Liu, F. Wang, H. Meng, and R. Liang, "Optical band-stop filter and multi-wavelength channel selector with plasmonic complementary aperture embedded in double-ring resonator," Photonics Nanostructures: Fundam. Appl. **23**, 45 (2017).
[32]A. Mouadili, E. H. El Boudouti, A. Soltani, A. Talbi, K. Haddadi, A. Akjouj, and B. Djafari-Rouhani, "Photonic demultiplexer based on electromagnetically induced transparency resonances," J. Phys. D: Appl. Phys. **52**, 075101 (2019).
[33]A. Mouadili, S. Khattou, M. Amrani, E. H. El Boudouti, N. Fettouhi, A. Talbi, A. Akjouj, and B. Djafari-Rouhani, "Y-shaped demultiplexer photonic circuits based on detuned stubs: Application to radiofrequency domain," Photonics **8**, 386 (2021).
[34]M. Amrani, S. Khattou, A. Noual, E. H. El Boudouti, and B. Djafari-Rouhani, "Plasmonic demultiplexer based on induced transparency resonances: Analytical and numerical study," Lect. Notes Electr. Eng. **681**, 239 (2021).
[35]Z. Zhu, C. E. Garcia-Ortiz, Z. Han, I. P. Radko, and S. I. Bozhevolnyi, "Compact and broadband directional coupling and demultiplexing in dielectric-loaded surface plasmon polariton waveguides based on the multimode interference effect," Appl. Phys. Lett. **103**, 061108 (2013).
[36]M. Amrani, S. Khattou, Y. Rezzouk, A. Mouadili, A. Noual, E. H. El Boudouti, and B. Djafari-Rouhani, "Analytical and numerical study of T-shaped plasmonic demultiplexer based on Fano and induced transparency resonances," J. Phys. D: Appl. Phys. **55**, 075106 (2022).
[37]X. Piao, S. Yu, and N. Park, "Control of Fano asymmetry in plasmon induced transparency and its application to plasmonic waveguide modulator," Opt. Express **20**, 18994 (2012).
[38]J. Chen, Z. Li, Y. Zou, Z. Deng, J. Xiao, and Q. Gong, "Coupled-resonator-induced Fano resonances for plasmonic sensing with ultra-high figure of merits," Plasmonics **8**, 1627 (2013).
[39]J. Chen, C. Wang, R. Zhang, and J. Xiao, "Multiple plasmon-induced transparencies in coupled-resonator systems," Opt. Lett. **37**, 5133 (2012).
[40]Z. Zhang, J. Yang, X. He, Y. Han, J. Huang, and D. Chen, "Tunable plasmon-induced transparency and slow light in terahertz chipscale semiconductor plasmonic waveguides," J. Phys. D: Appl. Phys. **53**, 315101 (2020).
[41]L. Dobrzynski, A. Akjouj, E. H. El Boudouti, G. Lévêque, H. Al-Wahsh, Y. Pennec, C. Ghouila-Houri, A. Talbi, B. Djafari-Rouhani, and Y. Jin, *Photonics* (Elsevier, Amsterdam, 2020).
[42]J. O. Vasseur, A. Akjouj, L. Dobrzynski, B. Djafari-Rouhani, and E. H. El Boudouti, "Photon, electron, magnon, phonon and plasmon mono-mode circuits," Surf. Sci. Rep. **54**, 1 (2004).
[43]G. J. Schneider, S. Hanna, J. L. Davis, and G. H. Watson, "Defect modes in coaxial photonic crystals," J. Appl. Phys. **90**, 2642 (2001).
[44]E. H. El Boudouti, N. Fettouhi, A. Akjouj, B. Djafari-Rouhani, A. Mir, J. O. Vasseur, L. Dobrzynski, and J. Zemmouri, "Experimental and theoretical evidence for the existence of photonic bandgaps and selective transmissions in serial loop structures," J. Appl. Phys. **95**, 1102 (2004).
[45]J. Arias, A. Sánchez-Meroño, M. M. Sánchez-López, and I. Moreno, "Slow and fast light in three-beam interferometers: Theory and experiment," Phys. Rev. A **85**, 033815 (2012).
[46]M. Bazargani, B. Gharekhanlou, and M. Banihashemi, "Design of optical 2-channel demultiplexer using selective optofluidic infiltration within photonic crystal structure," Radioengineering **29**, 3 (2020).
[47]G. Delphi, S. Olyaee, M. Seifouri, and A. Mohebzadeh-Bahabady, "Design of an add filter and a 2 channel optical demultiplexer with high quality factor based on nanoring resonator," J. Comput. Electron. **18**, 1372 (2019).
[48]S. A. Maier, *Plasmonics: Fundamentals and Applications* (Springer, 2007).
[49]M. Zhang and Z. Wang, "Analytical method for metal-insulator-metal surface plasmon polaritons waveguide networks," Opt. Express **27**, 303 (2019).
[50]H. U. Yang, J. D'Archangel, M. L. Sundheimer, E. Tucker, G. D. Boreman, and M. B. Raschke, "Optical dielectric function of silver," Phys. Rev. B **91**, 235137 (2015).
[51]L. Niu, Y. Xiang, W. Luo, W. Cai, J. Qi, X. Zhang, and J. Xu, "Nanofocusing of the free-space optical energy with plasmonic Tamm states," Sci. Rep. **6**, 39125 (2016).
[52]S. Naghizadeh and S. E. Kocabas, "Guidelines for designing 2D and 3D plasmonic stub resonators," JOSA B **34**, 207–217 (2017).
[53]Z. Zhang, J. Yang, X. He, J. Zhang, J. Huang, D. Chen, and Y. Han, "Plasmonic refractive index sensor with high figure of merit based on concentric-rings resonator," Sensors **18**, 116 (2018).
[54]M. R. Rakhshani and M. A. Mansouri-Birjandi, "Dual wavelength demultiplexer based on metal insulator metal plasmonic circular ring resonators," J. Mod. Opt. **63**, 1078 (2016).
[55]R. Zafar, P. Chauhan, M. Salim, and G. Singh, "Metallic slit loaded ring resonator based plasmonic demultiplexer with large crosstalk," Plasmonics **63**, 1013 (2019).
[56]E. Rafiee, R. Negahdari, and F. Emami, "Plasmonic multi channel filter based on split ring resonators: Application to photothermal therapy," Photonics Nanostructures: Fundam. Appl. **33**, 21 (2019).
[57]M. A. Butt, S. N. Khonina, and N. L. Kazanskiy, "A multichannel metallic dual nano-wall square split-ring resonator: Design analysis and applications," Laser Phys. Lett. **16**, 126201 (2019).